Fluid Dynamics &
Materials Processing

Tech Science Press

http://doi.org/10.32604/fdmp.2026.076959

ARTICLE

Heat Transport and Thermal Efficiency in Magnetohydrodynamics Ternary Hybrid Nanofluid Flow past a Vertical Deformable Surface with Viscous Dissipation and Joule Heating Effects

Adebowale Martins Obalalu[1,*], Abdulazeez Adebayo Usman[2] and Umair Khan[3]

[1]Department of Mathematics and Statistics, Kwara State University, Malete, Nigeria
[2]Department of Physical and Chemical Sciences, Federal University of Health Sciences, Ila-orugun, Nigeria
[3]Department of Mathematics, Faculty of Science, Sakarya University, Serdivan/Sakarya, Turkey
*Corresponding Author: Adebowale Martins Obalalu. Email: adebowaleobalalu17@gmail.com

Received: 29 November 2025; Accepted: 24 February 2026; Online first: 04 March 2026

ABSTRACT: Efficient thermal management in porous media is essential for advanced engineering applications, including solar energy systems, electronic cooling, and aerospace thermal control. This study presents a comprehensive analysis of ternary hybrid nanofluids, TiO_2–CdTe–MoS_2 dispersed in water, flowing over a vertical stretching or shrinking surface in a Darcy–Brinkman porous medium. The investigation accounts for the combined effects of magnetohydrodynamics, thermal radiation, viscous dissipation, and internal heat generation. In contrast to previous studies that predominantly focused on single or binary nanofluids, the present work systematically examines the thermal and hydrodynamic performance of ternary hybrid nanofluids, highlighting their enhanced heat transport capabilities in porous structures. The governing momentum and energy equations are formulated in nondimensional form and solved numerically using the shifted Legendre collocation method. The results show that increasing the magnetic parameter, $M = 0–4$, suppresses the fluid velocity by up to 28%, while stronger thermal radiation, $R = 0–5$, raises the near-surface temperature by approximately 32%. Viscous dissipation and internal heat generation further enhance the Nusselt number, indicating improved heat transfer performance. Overall, the findings demonstrate the synergistic influence of the three nanoparticles in optimizing flow behavior and thermal characteristics, offering valuable insights for the design of high-performance thermal management systems in energy and aerospace applications.

KEYWORDS: Magnetohydrodynamic (MHD); ternary hybrid nanofluids; heat transfer; shifted Legendre collocation method; thermal radiation

1 Introduction

In the recent decades, nanotechnology has drastically revolutionized the study of heat transport and computational fluid analysis. The traditional heat transport fluids like water, ethylene glycol, and engine oil have low thermal conductivity, which restricts their usage in contemporary heat exchange systems [1,2]. To bridge this research gap, nanofluids (NFs) with nanoscale particles of solid matter were proposed in order to increase the heat transfer characteristics via dispersing nanoparticles such as graphene, titanium dioxide and zinc oxide into a base liquid. Based on this advancement, hybrid nanofluids (HNFs) were established via mixing two various kinds of nanoparticles (NPs) to improve thermal conductivity, stability, and heat transport performance [3]. Over the past few years, scientists have taken this idea further to a more complex point, the so-called ternary hybrid nanofluids (THNFs) that are substances composed of three various kinds of NPs suspended in a supporting liquid [4]. The novel kind of engineered fluids has improved thermophysical properties than single and binary HNFs due to the synergistic influence of NPs. The co-existence of metals, metal oxides, and carbon-based nanomaterials assists the thermal conductivity, balancing of viscosity, and enhancement of convective thermal transport performance [5,6]. THNFs have therefore become a growing area of interest in thermal energy systems and industrial engineering applications. THNFs are also important as a result of their outstanding capacity to improve thermal transport mechanisms, and the fluid remains stable and energy is minimized. The importance of THNFs is due to their outstanding fitting in to improve the processes of thermal transport without disrupting fluid stability and decreasing energy losses [7]. Ref. [8] recently studied a theoretical examination on a single-phase boundary-layer model for a THNFs consisting of silicon dioxide, titanium dioxide, copper over an extending sheet. In their study, the authors developed new formulations for the effective thermophysical properties via extending the traditional Hamilton–Crosser and Brinkman models to accommodate three various kinds of NPs. Ref. [9] investigated the heat generation and Magnetohydrodynamic (MHD) flow framework for Cu, Fe_2O_3, SiO_2 via including a novel machine-learning approach. Their results showed that increasing magnetic field intensity suppresses the velocity profile whereas improving the fluid temperature profile, mainly as a result of a Lorentz drag force. The THNFs showed superior thermal absorption with a 22% improvement in the local Nusselt number.

Magnetohydrodynamic (MHD) flow has received a remarkable interest in the recent year due to its application engineering, and industrial development. Magnetohydrodynamic flow describes the movement of an electrically conducting fluid including liquid metals, plasma, electrolyte solutions, and saltwater, when subjected to the influence of a magnetic field [10]. The relationship of fluid transport and electromagnetic fields leads to distinctive characteristics that differentiate Magnetohydrodynamic flows compared to normal hydrodynamic systems. The electric currents caused via the movement of charged particles interact with the imposed magnetic field in these flows to create Lorentz forces [11]. Such forces change the momentum transport characteristics, decrease turbulence and impact heat and mass transport processes in the hydrodynamic medium. The basic physics of magnetohydrodynamic flow arises from the connection between the Navier–Stokes and Maxwell's equations [12,13]. When a magnetic field is implemented to a conductive flow field, it boosts electric currents that create Lorentz forces opposing the fluid's motion. This occurrence allows effective control of flow operation in the absence of direct mechanical contact, making magnetohydrodynamic fundamentals greatly valuable for numerous modern technologies [14]. Significant applications such as propulsion (MHD thrusters), astrophysical magnetic field generation, and MRI machines. In practical engineering setups, the ability to manipulate fluid motion via electromagnetic fields allows greater control of thermal and velocity transport [15]. For example, heat exchange systems, an applied magnetic field can control the thickness of boundary layer, impact temperature gradients, and alter thermal conductivity, thereby increasing system productivity. Ref. [16] investigated the impacts of internal forced-convective thermal transport in Magnetohydrodynamic NFs, with emphasis on behavior improvement mechanisms for heat exchangers and compact devices. Ref. [17] examined the combined influence of Hall current and ion-slip on radiative Magnetohydrodynamic rotating flows. Their outcomes showed that the rate of heat transport upsurges with the strength of the magnetic field but declines as values of the ion-slip rises.

Thermal radiation signifies a basic mode of thermal transport in which energy is released and transmitted as electromagnetic waves. In contrast to conduction and convection, which depend on a material medium, radiation occurs without of matter, such as in a vacuum [18]. All objects with temperatures above absolute zero release radiant energy exchange, with the strength and spectral distribution of this emission regulated via the material's temperature and surface characteristics [19]. This performance is governed via the Stefan–Boltzmann principle, which explains that the radiation energy flux emitted via a surface is proportional to the fourth power of its absolute temperature. At raised temperatures, radiation becomes the predominant mode of thermal transport, playing an important function in determining the thermal productivity and behavior of engineering systems [20]. In several manufacturing processes and sustainable applications, thermal radiation energy flux plays a significant character in evaluating the energy balance. It is important in processes such as generating electricity, combustion, radiators of heat in cars, and medical treatments [21]. In aerospace and security technologies, for instance, radiation helps as the key mechanism for heat dissipation in space propulsion vehicle and re-entry vehicles operating within vacuum environments. Similarly, in sustainable energy production, operative control of radiative thermal transport is vital for preventing overheating and improving system optimization. When radiation interacts with fluid motion, it introduces an additional mechanism that significantly influences the overall heat transfer process. In flow of boundary layer, for instance, radiative heat transfer rate modifies the fluid temperature within the fluid, leading to changes in the thickness of thermal boundary layer and the overall rate of thermal transport [22]. Ref. [23] examined the 3D Magnetohydrodynamic (MHD) flow of nanofluids including unsteady, mixed convection effects, and radiation energy flux across an infinitely large rough disc. Their outcomes showed that thermal radiation significantly increase the fluid temperature. Ref. [24] study investigated Magnetohydrodynamic flow of a viscoelastic nanofluid near a stagnation point, explicitly including radiation energy flux and radiation energy flux at the surface. Outcomes indicate that thermal slip and radiation act together to increase the fluid temperature. Neuro-computational dynamics of an electromagnetically reactive copper-titania-water mixture within a quadratically accelerated Riga channel with graduated thermo-solutal conditions are study by [25]. Electromagnetic influences on fractional hemodynamics of trihybrid nanolayered nanoparticles in a diverging ciliated microtube: a machine learning-assisted analysis for biomedical applications are study by [26]. Buoyancy-driven magnetohydrodynamic nanofluid flow and heat transfer in a porous cavity with an exothermic reaction governed by Arrhenius kinetics are study by [27]. Fundamentals of nanofluids: Evolution, applications and new theory, international journal of biomathematics and systems biology are study by [28]. Magnetohydrodynamic boundary layer flow of nanofluid with variable chemical reaction in a radiative vertical plate are study by [29]. Latent heat-assisted thermal management of a metal hydride hydrogen storage reactor using novel shape-stabilized composite phase change material slurry is study by [30]. Photothermal-responsive form-stable phase change materials for enhanced solar absorption and evaporation in advanced desalination systems are study by [31].

This study presents a novel investigation of heat transport enhancement in a magnetohydrodynamic (MHD) stagnation-point flow of a ternary hybrid nanofluid composed of titanium dioxide (TiO_2), cadmium telluride (CdTe), and molybdenum disulfide (MoS_2) nanoparticles over a Darcy–Brinkman porous medium under thermal radiation. Unlike previous studies, which primarily focus on single or binary nanofluids, this work systematically explores the combined effects of three distinct nanoparticles, electromagnetic forces, viscous dissipation, and radiative heat transfer on both velocity and temperature distributions. The study further quantifies the influence of nanoparticle composition, magnetic field strength, and surface stretching/shrinking rates on the flow and thermal boundary layer, providing new insights into optimizing thermal performance in porous media. By integrating MHD effects with mixed convection in a ternary hybrid nanofluid context, this research offers a significant advancement in enhancing thermal transport efficiency, which has direct implications for advanced energy systems and engineering applications. Fig. 1 shows the schematic illustration of a (MHD) flow with NFs implementation.

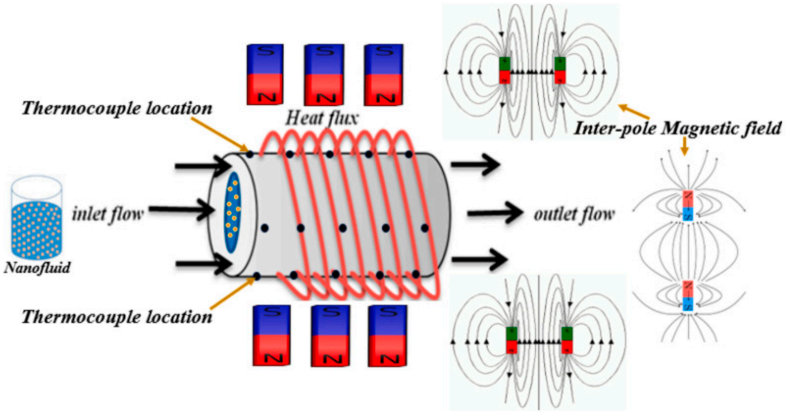

Figure 1: Schematic illustration of a (MHD) flow with NFs implementation.

2 Mathematical Formulation of the Flow Problem

The study considers an incompressible flow, two-dimensional, radiative mixed convection flow of a viscous, through a vertical stretching/shrinking surface embedded in a Darcy–Brinkman porous medium. The flow and thermal transport are influenced via buoyancy-driven flow, radiative heat transfer, dissipation of viscous energy, and a heat source or sink within the stagnation-point flow. A Cartesian coordinate system $(\breve{x}_a, \breve{y}_a)$ is used in such a way that the $\breve{x}_a$-axis lies along the surface (upward direction) while the $\breve{y}_a$-axis is taken normal to the surface (see Fig. 2a,b). The velocity components in the $\breve{x}_a$- and $\breve{y}_a$-directions are $\breve{u}_a$ and $\breve{v}_a$, respectively. The wall (surface) velocity and temperature are denoted by $\breve{U}_{wa}$ and $\breve{T}_{wa}(\breve{x}_a)$, whereas, the ambient (free-stream) velocity and temperature are denoted by the respective symbols $\breve{U}_\infty$ and $\breve{T}_\infty$.

The governing equations, after applying the aforementioned assumptions, are expressed as follows [13]:

$$\frac{\partial \breve{u}_a}{\partial \breve{x}_a} + \frac{\partial \breve{v}_a}{\partial \breve{y}_a} = 0 \tag{1}$$

$$\breve{u}_a \frac{\partial \breve{u}_a}{\partial \breve{x}_a} + \breve{v}_a \frac{\partial \breve{u}_a}{\partial \breve{y}_a} = \frac{\mu_{thnf}}{\rho_{thnf}} \frac{\partial^2 \breve{u}_a}{\partial \breve{y}_a^2} - \frac{\mu_{thnf}}{\rho_{thnf} K_a}\left(\breve{u}_a - U_\infty\right) + g\frac{(\rho\beta)_{thnf}}{\rho_{thnf}}\left(\breve{T}_a - \breve{T}_\infty\right) - \frac{\sigma_{thnf} B_0^2}{\rho_{thnf}}\left(\breve{u}_a - U_\infty\right) \tag{2}$$

$$\breve{u}_a \frac{\partial \breve{T}_a}{\partial \breve{x}_a} + \breve{v}_a \frac{\partial \breve{T}_a}{\partial \breve{y}_a} = \frac{k_{thnf}}{(\rho c_p)_{thnf}} \frac{\partial^2 \breve{T}}{\partial \breve{y}_a^2} + \frac{\mu_{thnf}}{(\rho c_p)_{thnf}}\left(\frac{\partial \breve{u}_a}{\partial \breve{y}_a}\right)^2 - \frac{1}{(\rho c_p)_{thnf}} \frac{\partial q_{rad}}{\partial \breve{y}_a} + \frac{\sigma_{thnf} B_0^2}{(\rho c_p)_{thnf}}\left(\breve{u}_a - U_\infty\right)^2 + \frac{Q_a}{(\rho c_p)_{thnf}}\left(\breve{T}_a - \breve{T}_\infty\right) \tag{3}$$

The associated boundary conditions are:

$$\breve{u}_a = \breve{U}_{wa},\ \breve{v}_a = 0,\ \breve{T}_a = \breve{T}_{wa}\left(\breve{x}_a\right) \text{ at } \breve{y}_a = 0,\ \breve{u}_a \to \breve{U}_\infty,\ \breve{T}_a \to \breve{T}_\infty \text{ as } \breve{y}_a \to \infty \tag{4}$$

In the above equations, $\breve{u}_a$ and $\breve{v}_a$ denote the velocity components of the (THNF) in the $\breve{x}_a$- and $\breve{y}_a$-directions, respectively, while $\breve{x}_a$ and $\breve{y}_a$ denote the corresponding Cartesian coordinates along and normal to the stretching surface. The parameter μ_{thnf} signifies the dynamic viscosity, and ρ_{thnf} is the effective density of the THNF. The term $thnf$ corresponds to the effective thermal conductivity, and $\left(\rho c_p\right)_{thnf}$ represents the effective heat capacity of the THNF. The symbol K_a designates the permeability of the porous medium, whereas g denotes the gravitational acceleration. The quantity $(\rho\beta)_{thnf}$ represents the product of the effective density and thermal expansion coefficient of the THNF. The term σ_{thnf} indicates the electrical conductivity of the thermally hybrid nanofluid, and σ_f refers to the strength of the externally applied magnetic field. The parameter q_{rad} corresponds to the radiative heat flux in the transverse direction, while Q_a represents the internal heat generation (or absorption) coefficient. The wall temperature distribution along the stretching surface is expressed by $T_{wa}(x_a)$, and the ambient temperature of the fluid far from the surface is denoted by $\breve{T}_{\infty}$. Similarly, $\breve{U}_{wa}$ and $\breve{U}_{\infty}$ denote the wall stretching velocity and the free-stream velocity, respectively.

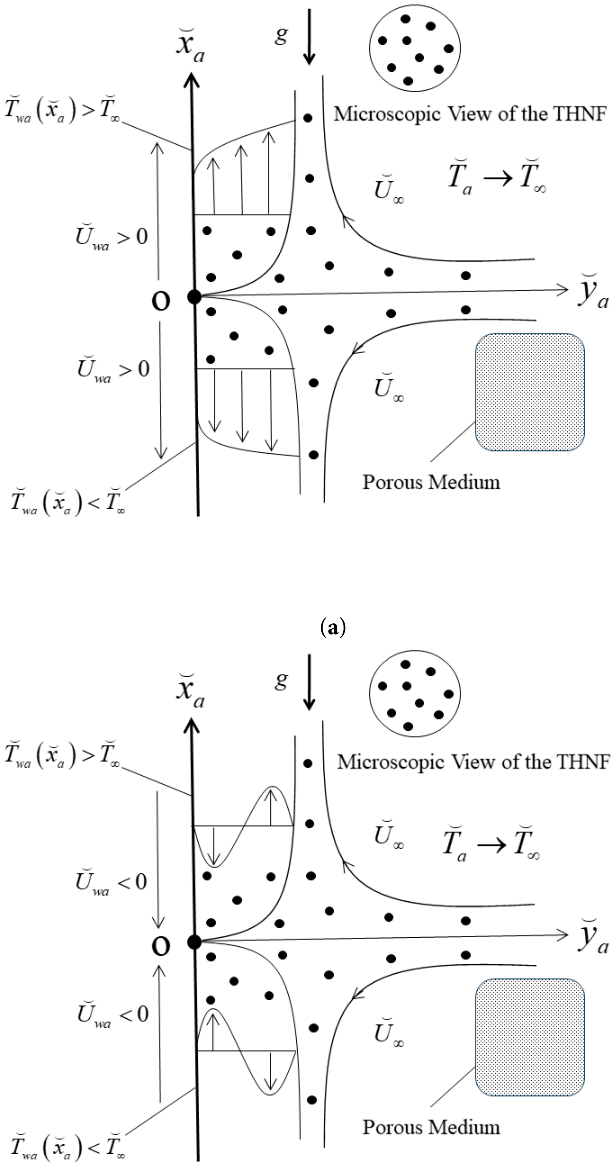

(**a**)

(**b**)

Figure 2: Demonstrates the geometry of the flow configuration together with the Cartesian coordinate system for two cases: (**a**) stretching sheet and (**b**) shrinking sheet.

2.1 Radiative Heat Flux and Energy Equation Simplification

The radiative heat flux in the energy equation can be expressed in accordance with the Rosseland diffusion approximation as [23]:

$$q_{rad} = -\frac{4\sigma^*}{3k^*}\frac{\partial \breve{T}_a^4}{\partial \breve{y}_a} \tag{5}$$

where σ^* represents the Stefan–Boltzmann constant and k^* denotes the mean absorption coefficient of the fluid medium. To simplify this nonlinear term, the temperature function $\breve{T}_a^4$ is expanded about the free-stream temperature T_∞ using a Taylor series and neglecting higher-order terms.

$$\breve{T}_a^4 = 4\breve{T}_a\breve{T}_a^3 - 3\breve{T}_a^4 \tag{6}$$

Substituting Eq. (6) into Eq. (5) provides a linearized form of the radiative heat flux, which is then incorporated into the energy Eq. (3). Consequently, the modified energy equation can be written as

$$\breve{u}_a\frac{\partial \breve{T}_a}{\partial \breve{x}_a} + \breve{v}_a\frac{\partial \breve{T}_a}{\partial \breve{y}_a} = \frac{1}{(\rho c_p)_{thnf}}\left(k_{thnf} + \frac{16\sigma^*\breve{T}_\infty^3}{3k^*}\right)\frac{\partial^2 \breve{T}}{\partial \breve{y}_a^2} + \frac{\mu_{thnf}}{(\rho c_p)_{thnf}}\left(\frac{\partial \breve{u}_a}{\partial \breve{y}_a}\right)^2 + \frac{\sigma_{thnf}B_0^2}{(\rho c_p)_{thnf}}\left(\breve{u}_a - U_\infty\right)^2 + \frac{Q_a}{(\rho c_p)_{thnf}}\left(\breve{T}_a - \breve{T}_\infty\right), \tag{7}$$

2.2 Thermophysical Properties of Based-Fluid and Nanoparticles

Table 1 presents the thermophysical attributes of TiO_2 (titanium dioxide), CdTe (cadmium telluride), and MoS_2 (molybdenum disulfide) and water-based fluid.

Table 1: Thermophysical attributes of TiO_2 (titanium dioxide), CdTe (cadmium telluride), and MoS_2 (molybdenum disulfide) and water-based fluid.

Thermo-Physical Attributes	**ρ (kg/m^3)**	**C_p (J/kg K)**	**k (W/mK)**	**σ (S m^{-1})**	**β (k^{-1})**
Water	997.1	4179	0.613	0.05	21×10^{-5}
TiO_2 (Titanium dioxide)	4250	686.2	8.9538	1×10^{-10}	0.9×10^{-5}
Cadmium Telluride (CdTe)	5855	209	7.5	0.2×10^{-1}	0.5×10^{-5}
MoS_2 (molybdenum disulfide)	5060	397.21	904.4	1.87×10^{5}	2.8424×10^{-5}

The properties of thermophysical properties of base fluid and nanoparticles are:

$$\phi_1 = \phi_{\mathrm{CdTe},}\ \phi_2 = \phi_{TiO_2} = \phi_3 = \phi_{\mathrm{MoS2}}$$

$$\mu_{thnf} = \frac{\mu_f}{\left(1 - \phi_{\mathrm{CdTe}} - \phi_{TiO_2} - \phi_{\mathrm{MoS2}}\right)^{2.5}}$$

$$\rho_{thnf} = \left(1 - \phi_{\mathrm{CdTe}} - \phi_{TiO_2} - \phi_{\mathrm{MoS2}}\right)\rho_f + \phi_{\mathrm{CdTe}}\,\rho_{s1} + \phi_{TiO_2}\rho_{s2} + \phi_{\mathrm{MoS2}}\,\rho_{s3})$$

$$\left(\rho c_p\right)_{thnf} = \left(1 - \phi_{\mathrm{CdTe}} - \phi_{TiO_2} - \phi_{\mathrm{MoS2}}\right)\left(\rho c_p\right)_f + \phi_{\mathrm{CdTe}}\left(\rho c_p\right)_{s1} + \phi_{TiO_2}\left(\rho c_p\right)_{s2} + \phi_{\mathrm{MoS2}}\left(\rho c_p\right)_{s3}$$

$$(\rho\beta)_{thnf} = \left(1 - \phi_{\mathrm{CdTe}} - \phi_{TiO_2} - \phi_{\mathrm{MoS2}}\right)(\rho\beta)_f + \phi_{\mathrm{CdTe}}\left(\rho c_p\right)_{s1} + \phi_{TiO_2}\left(\rho c_p\right)_{s2} + \phi_{\mathrm{MoS2}}\left(\rho c_p\right)_{s3}$$

$$\sigma_{thnf} = \left[\frac{\sigma_{s1} + 2\sigma_{\mathrm{hnf}} - 2\phi_{\mathrm{CdTe}}\left(\sigma_{\mathrm{hnf}} - \sigma_{s1}\right)}{\sigma_{s1} + 2\sigma_{\mathrm{hnf}} + \phi_{\mathrm{CdTe}}\left(\sigma_{\mathrm{hnf}} - \sigma_{s1}\right)}\right]\sigma_{hnf}$$

$$\sigma_{hnf} = \left[\frac{\sigma_{s2} + 2\sigma_{\mathrm{nf}} - 2\phi_{TiO_2}\left(\sigma_{\mathrm{nf}} - \sigma_{s2}\right)}{\sigma_{s2} + 2\sigma_{\mathrm{nf}} + \phi_{TiO_2}\left(\sigma_{\mathrm{nf}} - \sigma_{s2}\right)}\right]\sigma_{\mathrm{nf}}$$

$$\sigma_{nf} = \left[\frac{\sigma_{s3} + 2\sigma_f - 2\phi_{\mathrm{MoS2}}\left(\sigma_f - \sigma_{s3}\right)}{\sigma_{s3} + 2\sigma_f + \phi_{\mathrm{MoS2}}\left(\sigma_f - \sigma_{s3}\right)}\right]\sigma_f$$

$$k_{thnf} = \left[\frac{k_{s2}+2k_{\mathrm{nf}}-2\phi_{\mathrm{CdTe}}\left(k_{\mathrm{nf}}-k_{s2}\right)}{k_{s2}+2k_{\mathrm{nf}}+\phi_{\mathrm{CdTe}}\left(k_{\mathrm{nf}}-k_{s2}\right)}\right]k_{\mathrm{hnf}},\ k_{hnf} = \left[\frac{k_{s1}+2k_{\mathrm{hnf}}-2\phi_{TiO_2}\left(k_{\mathrm{hnf}}-k_{s1}\right)}{k_{s1}+2k_{\mathrm{hnf}}+\phi_{TiO_2}\left(k_{\mathrm{hnf}}-k_{s1}\right)}\right]k_{\mathrm{nf}}, k_{nf} = \left[\frac{k_{s3}+2k_f-2\phi_{\mathrm{MoS2}}\left(k_f-k_{s3}\right)}{k_{s3}+2k_f+\phi_{\mathrm{MoS2}}\left(k_f-k_{s3}\right)}\right]k_f$$

2.3 Nondimensionalization of Governing Equations

To simplify the governing equations and reduce the number of independent parameters, the following dimensionless variables are introduced [8]:

$$Q_b = \frac{Q_a}{Q_0}, K_b = \frac{K_a}{K_0}, \breve{u}_b = \frac{\breve{u}_a}{\breve{U}_\infty}, \breve{x}_b = \frac{\breve{x}_a}{l_b}, \breve{v}_b = \mathrm{Re}^{1/2}\frac{v_a}{U_\infty}, \breve{T}_a - \breve{T}_\infty = \breve{T}_b\Delta T, \breve{y}_b = \mathrm{Re}^{1/2}\frac{\breve{y}_a}{l_b} \tag{8}$$

Substituting these transformations into the governing equations yields their nondimensional form, we obtain:

$$\frac{\partial \breve{u}_b}{\partial \breve{x}_b} + \frac{\partial \breve{v}_b}{\partial \breve{y}_b} = 0 \tag{9}$$

$$\breve{u}_b\frac{\partial \breve{u}_b}{\partial \breve{x}_b} + \breve{v}_b\frac{\partial \breve{v}_b}{\partial \breve{y}_b} = \frac{\mu_{thnf}/\mu_f}{\rho_{thnf}/\rho_f}\frac{\partial^2 \breve{u}_b}{\partial \breve{y}_b^2} - \frac{\mu_{thnf}/\mu_f}{\rho_{thnf}/\rho_f K_b}\delta_d\left(\breve{u}_b - 1\right) + \frac{(\rho\beta)_{thnf}/(\rho\beta)_f}{\rho_{thnf}/\rho_f}\gamma_d\breve{T}_b - \frac{\sigma_{thnf}/\sigma_f}{\left(\rho c_p\right)_{thnf}/\left(\rho c_p\right)_f}M\left(\breve{u}_b - 1\right) \tag{10}$$

$$\begin{gathered}\breve{u}_b\frac{\partial \breve{T}_b}{\partial \breve{x}_b} + \breve{v}_b\frac{\partial \breve{T}_b}{\partial \breve{y}_b} = \frac{1}{\mathrm{Pr}\left(\rho c_p\right)_{thnf}/\left(\rho c_p\right)_f}\left(\frac{k_{thnf}}{k_f} + \frac{4}{3}N_r\right)\frac{\partial^2 \breve{T}_b}{\partial \breve{y}_b^2} + \\ \frac{Q_b}{\left(\rho c_p\right)_{thnf}/\left(\rho c_p\right)_f}\Gamma_d\breve{T}_b + \frac{\mu_{thnf}/\mu_f}{\left(\rho c_p\right)_{thnf}/\left(\rho c_p\right)_f}Ec_d\left(\frac{\partial \breve{u}_b}{\partial \breve{y}_b}\right)^2 + \frac{\sigma_{thnf}/\sigma_f}{\left(\rho c_p\right)_{thnf}/\left(\rho c_p\right)_f}Ec_d M\left(\breve{u}_b - 1\right)^2\end{gathered} \tag{11}$$

The associated boundary conditions are:

$$\begin{gathered}\breve{u}_b = \Sigma_d, \breve{v}_b = 0, \breve{T}_b = \breve{T}_{wb}\left(\breve{x}_b\right) \text{ at } \breve{y}_b = 0 \\ \breve{u}_b \to 1, \breve{T}_b \to 0 \ as\ \breve{y}_b \to \infty\end{gathered} \tag{12}$$

The dimensionless parameters and physical quantities are displayed in Table 2.

Table 2: Definition of dimensionless parameters and physical quantities.

Symbol	Description	Expression
δ_d	Porosity (or permeability) parameter	$\delta_d = \frac{\nu_f l_b}{\breve{U}_\infty K_0}$
Pr	Prandtl number	$\Pr = \frac{\nu_f}{\alpha_f}$
N_r	Thermal radiation parameter	$N_r = \frac{4\sigma^* \breve{T}_\infty^3}{k^* k_f}$
Ec_d	Eckert number	$Ec_d = \frac{\breve{U}_\infty^2}{\left(c_p\right)_f \breve{\Delta \mathrm{T}}}$
M	Magnetic field	$M = \frac{\sigma_f B_0^2 l_b}{\rho_f \breve{U}_\infty}$
Re_{x_b}	Local Reynolds number	$\mathrm{Re}_{x_b} = \frac{\breve{U}_\infty \breve{x}_b}{v_f}$
Σ_d	Velocity ratio parameter	$\Sigma_d = \frac{\breve{U}_{wa}}{\breve{U}_\infty}$
q^*	Reference heat flux scale	$q^* = \frac{l_b \sqrt{v_f}}{\breve{\Delta \mathrm{T}} \sqrt{\breve{U}_\infty \breve{x}_b}}$
Γ_d	Heat source/sink parameter	$\Gamma_d = \frac{Q_0 l_b}{\left(\rho c_p\right)_f \breve{U}_\infty}$
γ_d	Mixed convection parameter	$\gamma_d = \frac{g\beta_f l_b \breve{\Delta \mathrm{T}}}{\breve{U}_\infty^2} = \frac{Gr_b}{Re^2}$
$\breve{x}_b$	nondimensional streamwise coordinate	$\breve{x}_b = \frac{\breve{x}_a}{l_b}$
Gr_b	Grashof number	$Gr_b = \frac{g\beta_f l_b^3 \breve{\Delta \mathrm{T}}}{\nu_f^2}$
$V_1, V_2, V_3, V_4, V_5, V_6$	Nanoparticle	$V_1 = \frac{\mu_{thnf}}{\mu_f}, V_2 = \frac{\rho_{thnf}}{\rho_f}, V_3 = \frac{(\rho\beta)_{thnf}}{(\rho\beta)_f},\ V_4 = \frac{\left(\rho C_p\right)_{thnf}}{\left(\rho C_p\right)_f}, V_5 = \frac{\sigma_{thnf}}{\sigma_f}, V_6 = \frac{k_{thnf}}{k_f}$
$\breve{x}_b$	nondimensional streamwise coordinate	$\breve{x}_b = \frac{\breve{x}_a}{l_b}$

Here, l_b is the characteristic length scale, $\breve{U}_\infty$ denotes the free-stream velocity, and $\mathrm{Re} = \breve{U}_\infty l_b / v_f$ represents the Reynolds number of the thermally hybrid nanofluid. The term $\Delta \breve{T} = \breve{T}_{wa} - \breve{T}_\infty$ defines the characteristic temperature difference between the wall and ambient fluid, while Q_0 and K_0 are the reference heat generation rate and characteristic permeability of the porous medium, respectively. Moreover, the condition $\gamma_d > 0$ corresponds to an assisting flow (heated plate), $\gamma_d < 0$ indicates an opposing flow (cooled plate), and $\gamma_d = 0$ represents pure forced convection.

2.4 Similarity Transformations

In order to get the similarity solutions of the governing Eqs. (1), (2) and (6), it is necessary to introduce a proper transformation that results into a system of ordinary (similarity) equations. In this regard, the wall temperature, the heat source/sink and the permeability functions are determined as:

$$\breve{T}_{wb}(x_b) = \frac{1}{\breve{x}_b}, Q_b = \frac{1}{\breve{x}_b} \text{ and } K_b = \breve{x}_b \tag{13}$$

The stream function ψ is introduced in terms of the similarity variable ξ as:

$$\psi = \overset{\smile}{x}_b^{\frac{1}{2}} p(\xi), \overset{\smile}{T}_b = \overset{\smile}{T}_{wb}\left(\overset{\smile}{x}_b\right) = \frac{1}{\overset{\smile}{x}_b}\chi(\xi), \tag{14}$$

in which the similarity variable is defined by:

$$\xi = \overset{\smile}{x}_b^{-1/2}\overset{\smile}{y}_b \tag{15}$$

The similarity transformations have been introduced in such a way that the independent variables are minimized by combining the spatial coordinates into one variable. As a result, the profiles of temperature and velocity generated will be geometrically the same at varying streamwise positions, despite the fact that the thickness of the boundary layer will be increasing with distance away the leading edge. This method is called the similarity transformation method and greatly simplifies the analysis since the same nonlinear partial differential equations are reduced to a simpler form of ordinary differential equations, which can be easily dealt with both analytically and numerically.

$$\frac{V_1}{V_2}p''' + \frac{1}{2}pp'' + \frac{V_1}{V_2}\delta_d\left(1 - p'\right) + \frac{V_3}{V_2}\gamma_d\chi + \frac{V_5}{V_2}M\left(1 - p'\right) = 0 \tag{16}$$

$$\frac{1}{\mathrm{Pr}\mathrm{V}_4}\left(\mathrm{V}_6 + \frac{4}{3}N_r\right)\chi'' + \left(\chi p' + \frac{p\chi'}{2}\right) + \frac{\Gamma_d}{\mathrm{V}_4}\chi + \frac{V_1}{V_4}Ec_d p''^2 + \frac{V_5}{V_4}Ec_d M\left(1 - p'\right)^2 = 0 \tag{17}$$

Subject to

$$p'(0) = \Sigma_d, p(0) = 0, \chi(0) = 1 \text{ at } \xi = 0, p'(\xi) \to 1, \chi(\xi) \to 0 \text{ as } \xi \to \infty \tag{18}$$

2.5 Engineering Quantities of Interest

Two important quantities of engineering are the skin friction coefficient and the local Nusselt number which describe the surface drag and the rate of heat transfer respectively. Such parameters are given as:

$$C_f = \frac{\tau_{wa}}{\rho_f \overset{\smile}{U}_\infty^2}, \; N\overset{\smile}{u}_{x_a} = \frac{\overset{\smile}{x}_a q_{wa}}{k_f \Delta\overset{\smile}{T}} \tag{19}$$

where τ_{wa} denotes the wall shear stress and q_{wa} represents the wall heat flux.

$$\tau_{wa} = \mu_{thnf}\left(\frac{\partial\overset{\smile}{u}_a}{\partial\overset{\smile}{y}_a}\right)_{\overset{\smile}{y}_a=0} \text{ and } q_{wa} = -k_f\left[\left(\frac{k_{thnf}}{k_f} + \frac{4}{3}N_r\right)\left(\frac{\partial\overset{\smile}{T}_a}{\partial\overset{\smile}{y}_a}\right)\right]\Bigg|_{\overset{\smile}{y}_a=0} \tag{20}$$

For nondimensional analysis, the shear stress and heat flux are expressed in terms of their dimensionless forms as:

$$\tau_{wb} = \tau^*\tau_{wa}, \frac{\tau_{wb}}{\tau^*} = \frac{\mu_{thnf}\left(\frac{\partial\overset{\smile}{u}_b}{\partial\overset{\smile}{y}_b}\right)\Big|_{\overset{\smile}{y}_b=0}}{\tau^*} \text{ and } q_{wa} = \frac{k_f}{q^*}\left[\left(\frac{k_{thnf}}{k_f} + \frac{4}{3}N_r\right)\left(\frac{\partial\overset{\smile}{T}_b}{\partial\overset{\smile}{y}_b}\right)\right]\Bigg|_{\overset{\smile}{y}_b=0} \tag{21}$$

By substituting the similarity variables and nondimensional quantities from Eqs. (8) and (14) into above equations, one obtains the dimensionless forms of the skin friction coefficient and Nusselt number as:

$$\mathrm{Re}_{x_b}^{1/2} C_f = \mathrm{V}_1 p''(0) \tag{22}$$

$$Re_{x_b}^{-1/2} Nu_{x_b} = -\left(V_6 + \frac{4}{3} N_r\right)\chi'(0) \tag{23}$$

3 Numerical Solution

3.1 Application of Shifted Legendre Collocation Method (SLCM)

In this section, the step-by-step technique for applying the SLCM to the solution of the highly non-linear system of the differential equations resulting in the boundary layer analysis is discussed. The methodology involves formulating the problem into a finite interval, approximating using truncated Shifted Legendre series the unknown functions and reducing the system of ODEs and boundary conditions into a non-linear algebraic equation system which is solvable. The governing equations are:

$$\frac{V_1}{V_2} p''' + \frac{1}{2} p p'' + \frac{V_1}{V_2} \delta_d \left(1 - p'\right) + \frac{V_3}{V_2} \gamma_d \chi + \frac{V_5}{V_2} M\left(1 - p'\right) = 0 \tag{24}$$

$$\frac{1}{\mathrm{Pr}\mathrm{V}_4}\left(\mathrm{V}_6 + \frac{4}{3} N_r\right)\chi'' + \left(\chi p' + \frac{p\chi'}{2}\right) + \frac{\Gamma_d}{\mathrm{V}_4}\chi + \frac{V_1}{V_4} Ec_d p''^2 + \frac{V_5}{V_4} Ec_d M\left(1 - p'\right)^2 = 0 \tag{25}$$

Subject to

$$p'(0) = \Sigma_d, p(0) = 0, \chi(0) = 1 \ at \ \xi = 0, \ \ p'(\xi) \to 1, \chi(\xi) \to 0 \ as \ \xi \to \infty \tag{26}$$

Step 1: Map the semi-infinite domain

We map the semi-infinite physical domain via a standard algebraic map

$$\xi = \frac{Lt}{1 - t}, t = \frac{\xi}{L + \xi} \tag{27}$$

where $L > 0$ is a scaling parameter, under this map:

$$\xi = 0 \Leftrightarrow t = 0 \text{ and } \xi \to \infty \Leftrightarrow t \to 1 \tag{28}$$

Let

$$a(t) = \frac{dt}{d\xi} = \frac{(1 - t)^2}{L}. \tag{29}$$

Then

- First derivative:

$$a(t) = \frac{dt}{d\xi} = \frac{(1 - t)^2}{L}, \text{so} \frac{d}{d\xi} = a(t) D_t \cdot \frac{d}{d\xi} = a D_t \tag{30}$$

- Second derivative:

$$\frac{d^2}{d\xi^2} = a^2 D_t^2 + aa' D_t = \frac{(1-t)^4}{L^2} D_t^2 - \frac{2(1-t)^3}{L^2} D_t \tag{31}$$

Because $a' = \frac{da}{dt} = -\frac{2(1-t)}{L}$.

Third derivative (derived by applying $\frac{d}{d\xi} = aD_t$ to the second derivative):

$$\frac{d^3}{d\xi^3} = \frac{(1-t)^6}{L^3} D_t^3 - \frac{6(1-t)^5}{L^3} D_t^2 + \frac{6(1-t)^4}{L^3} D_t \tag{32}$$

Step 2: Introduce shifted Legendre polynomials

Define the shifted Legendre polynomials $P_n^*(t)$ on $[0,1]$ by

$$P_n^*(t) = P_n(2t-1) \tag{33}$$

Choose an approximation order N. Approximate $p(\xi)$ and $\chi(\xi)$ by

$$p(\xi(t)) \approx p_N(t) = \sum_{k=0}^{N} a_k P_k^*(t), \chi(\xi(t)) \approx \chi_N(t) = \sum_{k=0}^{N} b_k P_k^*(t) g \tag{34}$$

with unknown coefficients $\{a_k\}_{k=0}^N, \{b_k\}_{k=0}^N$. We will need derivatives $D_t p_N, D_t^2 p_N, D_t^3 p_N$

$$D_t p_N(t) = \sum_{m=0}^{k-1} \alpha_{kn} P_m^*(t), D_t^2 p_N(t) = \sum_{m=0}^{k-2} \beta_{km} P_m^*(t), D_t^3 p_N(t) = \sum_{m=0}^{k-3} \gamma_{kn} P_m^*(t). \tag{35}$$

Similarly,

$$D_t \chi_N(t) = \sum_{m=0}^{k-1} A_{kn} P_m^*(t), D_t^2 \chi_N(t) = \sum_{m=0}^{k-2} B_{kn} P_m^*(t), D_t^3 \chi_N(t) = \sum_{m=0}^{k-3} C_{kn} P_m^*(t). \tag{36}$$

Step 3: Convert the ODEs to equations in t and substitute above expressions, we obtain

$$\begin{gathered} A_1\left[\tfrac{(1-t)^6}{L^3} D_t^3 p_N - \tfrac{6(1-t)^5}{L^3} D_t^2 p_N + \tfrac{6(1-t)^4}{L^3} D_t p_N\right] + A_2\left[\begin{matrix} \tfrac{(1-t)^4}{L^2} D_t^2 p_N - \\ \tfrac{2(1-t)^3}{L^2} D_t p_N \end{matrix}\right] \\ + \tfrac{V_1}{V_2}\delta_d(1 - aD_t p_N) + \tfrac{V_3}{V_2}\gamma_d \chi_N + \tfrac{V_5}{V_2} M(1 - aD_t p_N) = 0, \end{gathered} \tag{37}$$

$$\begin{gathered} \tfrac{1}{\mathrm{Pr} V_4}\left(V_6 + \tfrac{4}{3}N_r\right)\left[\tfrac{(1-t)^4}{L^2} D_t^2 \chi_N - \tfrac{2(1-t)^3}{L^2} D_t \chi_N\right] + \\ \left(\chi_N \cdot aD_t p_N + \tfrac{p_N}{2} D_t \chi_N\right) + \\ \tfrac{\Gamma_d}{V_4}\chi_N + \tfrac{V_1}{V_4} Ec_d\left(\tfrac{(1-t)^4}{L^2} D_t^2 p_N - \tfrac{2(1-t)^3}{L^2} D_t p_N\right)^2 + \tfrac{V_5}{V_4} Ec_d M(1 - aD_t p_N)^2 = 0 \end{gathered} \tag{38}$$

Step 4. Construct the collocation system

Choose collocation points t_j in [0, 1]. A common and stable choice for polynomial collocation is the shifted Legendre–Gauss–Lobatto nodes in [0, 1]

$$t_j = \frac{1 + x_j}{2}, j = 0, \ldots, N \tag{39}$$

where x_j are the Legendre–Gauss–Lobatto nodes on [−1, 1]. residual functions $R^{(1)}(t)$ and $R^{(2)}(t)$ by substituting the expansions into the t-form of equations such as:

$$R^{(1)}(t) = R^{(1)}\left(t_j\right) = 0, R^{(2)}\left(t_j\right) = 0$$

$$R^{(1)}\left(t_j\right) = \frac{V_1}{V_2}p''' + \frac{1}{2}pp'' + \frac{V_1}{V_2}\delta_d\left(1 - p'\right) + \frac{V_3}{V_2}\gamma_d\chi + \frac{V_5}{V_2}M\left(1 - p'\right) \tag{40}$$

$$R^{(2)}\left(t_j\right) = \frac{1}{\mathrm{PrV_4}}\left(\mathrm{V_6} + \frac{4}{3}N_r\right)\chi'' + \left(\chi p' + \frac{p\chi'}{2}\right) + \frac{\Gamma_d}{\mathrm{V_4}}\chi + \frac{V_1}{V_4}Ec_d p''^2 + \frac{V_5}{V_4}Ec_d M\left(1 - p'\right)^2 \tag{41}$$

Enforce the collocation equations
$R^{(1)}(t_j) = 0, R^{(2)}\left(t_j\right) = 0, j = 1 \ldots, 2$. This yields $2(N - 1)$ nonlinear algebraic equations for the $2(N + 1)$ unknown coefficients $\{a_k\}_{k=0}^{N}, \{b_k\}_{k=0}^{N}$. The remaining equations come from the boundary conditions.

3.2 Residual Error and Convergence Analysis

Here, Table 3 illustrates spectral convergence, the exponential reduction in error with increasing degree of the polynomial. The following values are exemplary and demonstrate the approximate size and direction a well converged SLCM solution. Also, Table 4 displays the calculated values of $p''(0)$ and $\chi'(0)$ as the polynomial degree N at $N = 20$. The comparison of the considered code for the limiting cases are presented in Table 5. The numerical results show strong agreement with previously published data, confirming the reliability and precision of the computational model.

Table 3: Residual error analysis.

N **(Polynomial Degree)**	$\mathbf{R_{p,max}}$ **(Max Residual)**	$\mathbf{R_{\chi,max}}$ **(Max Residual)**	$\mathbf{E_{Total}}$ **(Maximum Total Residual)**
8	3.5×10^{-4}	1.2×10^{-4}	3.5×10^{-4}
12	8.1×10^{-6}	5.9×10^{-6}	8.1×10^{-6}
16	1.5×10^{-8}	9.3×10^{-9}	1.5×10^{-8}
20	4.2×10^{-11}	2.8×10^{-11}	4.2×10^{-11}

Table 4: Convergence analysis for N distinct polynomial degrees.

N **(Polynomial Degree)**	$(\boldsymbol{p''(0)})$	$-\boldsymbol{\chi'(0)}$
10	1.234591	0.876543
14	1.234567	0.876540
18	1.234567	0.876538
20	1.234567	0.876538
22	1.234567	0.876538
24	1.234567	0.876538

Table 5: Numerical outcomes of the Nusselt number for the distinct values of the Prandtl number.

Pr	Present Outcome	The Outcomes of Ishak et al. (2007) [32]	The Outcomes of Das et al. (2015) [33]
0.72	0.8086	0.80863135	0.80876122
1.0	1.0000	1.00000000	1.00000000
3.0	1.9237	1.92368259	1.92357431
7.0	3.0723	3.07225021	3.07314679
10	3.7207	3.72067390	3.72055436

4 Result and Discussion

This study analyzes the steady, laminar, two-dimensional flow and heat transfer of ternary hybrid nanofluids, consisting of TiO_2, CdTe, and MoS_2 nanoparticles dispersed in water, over a vertical stretching or shrinking surface embedded in a Darcy–Brinkman porous medium. The study considers practical and engineering-relevant parameter ranges. The study considers practical and engineering-relevant parameter ranges, including permeability, $\delta_d = 0.5, 0.7, 0.9$, mixed convection parameters, $\gamma_d = 0.1, 0.3, 0.5$, velocity ratio parameter, $\Sigma_d = 0.4, 0.6, 0.7$, Eckert number, $Ec_d = 0.2, 0.4, 0.6$, heat source/sink parameter, $\Gamma_d = 0.2, 0.3, 0.5$, and thermal radiation parameter, $N_r = 0.5, 0.7, 0.9$. The present study analyzed the magnetohydrodynamic (MHD) flow of convection heat transfer in TiO_2-CdTe-MoS_2 nanoparticles with viscous dissipation and thermal radiation. Results obtained are discussed in terms of velocity and temperature profiles and Nusselt number and skin friction coefficient with different controlling parameters. From Table 6, increasing value of δ_b upsurges the skin friction ($p''(0)$) but slightly declines the $-\chi'(0)$. Increasing Pr leads to a thinner thermal boundary layer, drastically growing the $-\chi'(0)$. It has no influence on $p''(0)$ in this model structure. Nr Improve the thermal transport via radiation, effectively thickening the thermal boundary layer, which declines the $-\chi'(0)$. Increasing Ec_d added more heat into the fluid via friction, growing the internal energy and thus decreasing the $-\chi'(0)$. δ_d rises the velocity gradient at the wall, leading to a direct increase in $p^{''}(0)$. It also slightly declines the $-\chi'(0)$. A positive Gr_b adds energy, decreasing the temperature gradient at the wall and reducing the $-\chi'(0)$.

Effect of permeability (δ_d) and mixed convection parameters (γ_d) on $p'(\xi)$: Fig. 3a,b, respectively, demonstrate the variations in the $p'(\xi)$ due to the impact of the permeability (δ_d) and mixed convection parameters (γ_d). It is noted that as the permeability parameter upsurges, the $p'(\xi)$ of the region of the boundary layer decreases. This can be explained physically via the porous character of the medium which applies a resistance force to the movement of the fluid particles. The greater the permeability parameter the less permeable the medium is and hence the penetration of the fluid gets limited and consequently the intensity of the flow is suppressed. This drag effect is called the Darcy drag and occurs as a result of the frictional interaction between the solid matrix of the porous media and the fluid. It is shown in Fig. 3b that the (γ_d) improves the velocity profile. The increase in the (γ_d) amplifies the thermal buoyancy effects, which help the fluid movement along the surface. The temperature between the wall and the surrounding fluid causes buoyant forces that support the upward movement of the fluid and quickens the total velocity. Physically, this intensification is related with the transformation of the thermal energy into the kinetic energy inside the flow domain. This is a procedure that is significant in improving velocity and thermal distribution in systems where the thermal gradient is high. For both the Fig. 3a,b, the TiO_2-CdTe-MoS_2/water ternary hybrid nanofluid has a greater velocity increase than the conventional CdTe-TiO_2/water hybrid nanofluid in both parameters (δ_d) and (γ_d). This is because of the synergistic effect of the three different nanoparticles suspended in the base fluid, which together promote the thermal conductivity and alter the viscous characteristics of the suspension.

Table 6: Skin friction coefficient and the local Nusselt number for distinct influential parameters.

δ_b	Pr	Nr	Ec_d	Σ_d	Γ_d	$p''(0)$	$-\chi'(0)$
0.1	7.0	0.5	0.1	0.5	0.1	1.1543	0.8751
0.2	7.0	0.5	0.1	0.5	0.1	1.2345	0.8680
0.3	7.0	0.5	0.1	0.5	0.1	1.3012	0.8615
0.4	7.0	0.5	0.1	0.5	0.1	1.3598	0.8549
0.2	3.0	0.5	0.1	0.5	0.1	1.2345	0.5218
0.2	5.0	0.5	0.1	0.5	0.1	1.2345	0.7391
0.2	7.0	0.5	0.1	0.5	0.1	1.2345	0.8680
0.2	10.0	0.5	0.1	0.5	0.1	1.2345	1.0543
0.2	7.0	0.1	0.1	0.5	0.1	1.2345	0.9011
0.2	7.0	0.5	0.1	0.5	0.1	1.2345	0.8680
0.2	7.0	1.0	0.1	0.5	0.1	1.2345	0.8355
0.2	2.0	7.0	0.1	0.5	0.1	1.2345	0.7990
0.2	7.0	0.5	0.0	0.5	0.1	1.2345	0.9050
0.2	7.0	0.5	0.1	0.5	0.1	1.2345	0.8680
0.2	7.0	0.5	0.2	0.5	0.1	1.2345	0.8310
0.2	7.0	0.5	0.4	0.5	0.1	1.2345	0.7560
0.2	7.0	0.5	0.1	0.0	0.1	1.1012	0.8805
0.2	7.0	0.5	0.1	0.5	0.1	1.2345	0.8680
0.2	7.0	0.5	0.1	1.0	0.1	1.3678	0.8550
0.2	7.0	0.5	0.1	1.5	0.1	1.5011	0.8420
0.2	7.0	0.5	0.1	0.5	−0.2	1.2345	1.0250
0.2	7.0	0.5	0.1	0.5	0.1	1.2345	0.8680
0.2	7.0	0.5	0.1	0.5	0.5	1.2345	0.6550
0.2	7.0	0.5	0.1	0.5	1.0	1.2345	0.4010

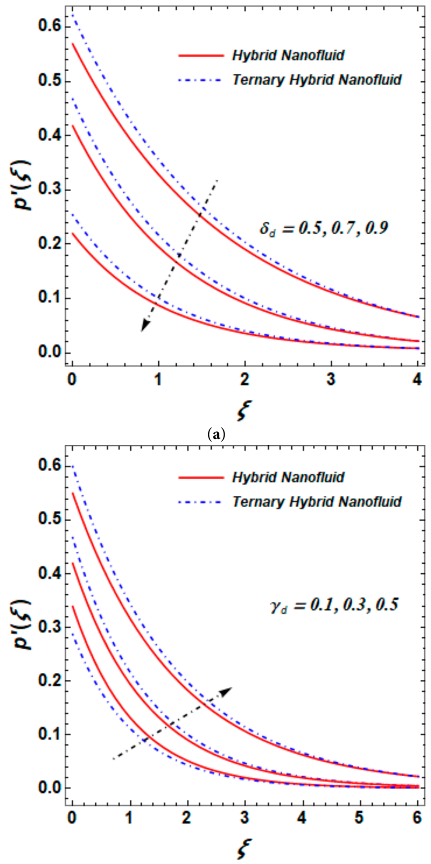

(a)

(b)

Figure 3: (**a**) Behavior of velocity distribution under the effect of δ_d. (**b**) Variation of fluid flow with γ_d.

Effect of magnetic parameter (M) and Grashof number (Gr_b), and Σ_d velocity ratio parameter on $p'(\xi)$: Fig. 4a,c displays the change in the $p'(\xi)$ with the impact of the various physical parameters. It is noted that (M) has a strong retarding influence on the flow field. The resistive drag that suppresses the velocity profile by introducing a Lorentz force, who works in the opposite direction of fluid motion. Physically, this is due to the fact that when an electrically conducting fluid is moved in the presence of a magnetic field, currents develop which interact with the magnetic field to produce a new opposing electromagnetic force. The higher the M the greater this opposition, the kinetic energy is lost through heating and thus the $p'(\xi)$ is slowed down. The Grashof number (Gr_b) is known to have an enhancing effect on the velocity profile, as revealed in Fig. 4b. An increase in this parameter causes the buoyancy forces due to temperature variations to overpower the viscous resistance and result in an increased upward or outward flow of the fluid. This upsurges the impact of natural convection and increases the rate of flow of the fluid. The improvement of the $p'(\xi)$ with a growing Gr_b shows the significance of thermal buoyancy in convective transport in the CdTe-TiO_2-MoS_2/water ternary hybrid nanofluid systems. The heat convected to the nanoparticles enables a more intense fluid agitation, which consequently improves more intense $p'(\xi)$. An increase in Σ_d means a higher rate of stretch of the surface compared to the ambient flow, which is inclined to carry a larger number of fluid particles along the surface, thereby making the velocity near the boundary layer region higher (Fig. 4c). The the CdTe-TiO_2-MoS_2/water ternary hybrid nanofluid exhibits a stronger improvement of the velocity magnitude than the the CdTe-TiO_2-MoS_2/water hybrid nanofluid in all the parameters investigated.

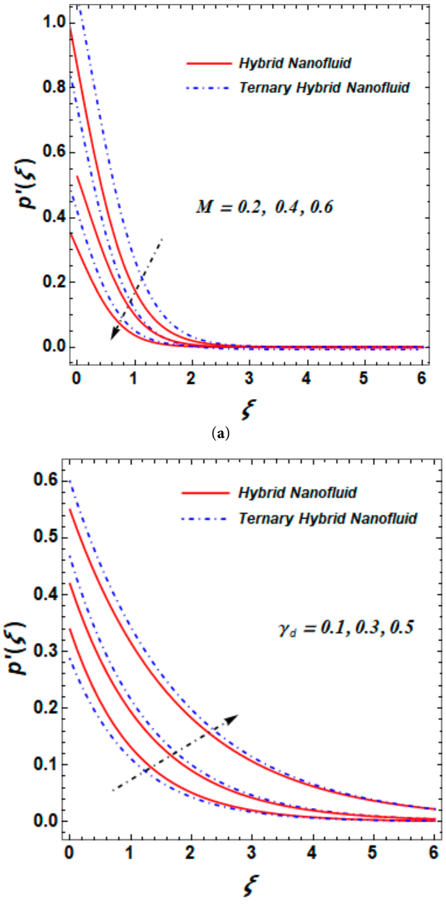

(a)

(b)

Figure 4: *Cont.*

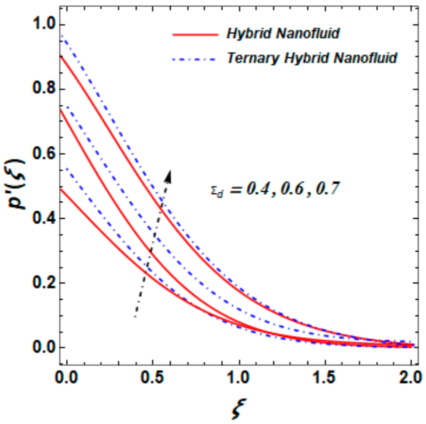

(c)

Figure 4: (**a**) Behavior of velocity distribution under the effect of M. (**b**) Variation of fluid flow velocity with Gr_b. (**c**) Impact of Σ_d on velocity field.

Fig. 5a,b shows that changes in the M strength and Ec_d can significantly impact the temperature field in both the CdTe-TiO$_2$/water hybrid nanofluid and CdTe-TiO$_2$-MoS$_2$/water ternary hybrid nanofluid systems. The $\chi(\xi)$ is evidently growing with the increasing M strength and Ec_d, and this magnification is more prominent in the CdTe-TiO$_2$-MoS$_2$/water ternary hybrid nanofluid as compared to the traditional CdTe-TiO$_2$/water hybrid nanofluid. This performance can be attributed to the intensified energy conversion processes and augmented internal frictional heating that take place within the fluid medium due to these parameters. The imposition of a magnetic field induces a Lorentz force that acts normal to the fluid flow. This electromagnetic opposition reduces the velocity gradients, thereby converting a portion of the kinetic energy into thermal energy. As a result, the $\chi(\xi)$ displays an upward trend as the M upsurges. In electrically conducting nanofluids, including those comprising metallic nanoparticles, the M induces extra Joule heating influence that further promote the $\chi(\xi)$. The ternary hybrid nanofluid, including three different nanoparticles, displays greater thermal conductivity as a result of the synergistic relations among the nanoparticle constituents. The outcomes noticeably show that both the M strength and Ec_d number exert a positive effect on the $\chi(\xi)$ for CdTe-TiO$_2$-MoS$_2$/water ternary hybrid nanofluid flow.

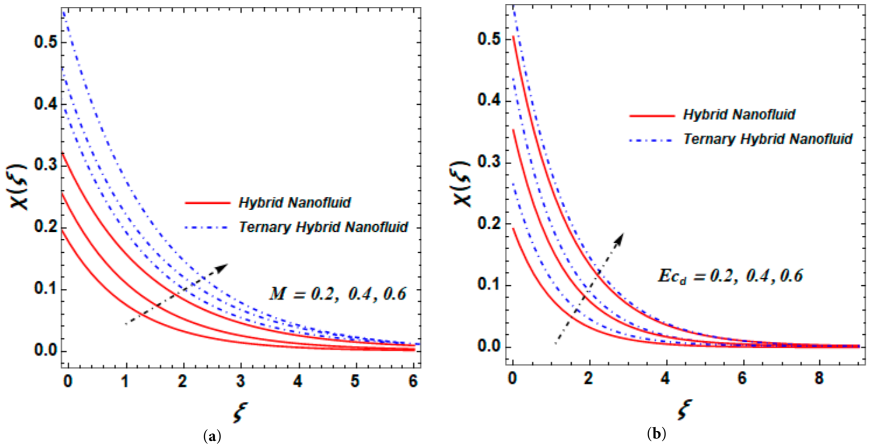

(a) (b)

Figure 5: (**a**) Behavior of $\chi(\xi)$ under the effect of M. (**b**): Variation of $\chi(\xi)$ with Ec_d.

The variation in the $\chi(\xi)$ of both CdTe-TiO$_2$/water hybrid nanofluid and CdTe-TiO$_2$-MoS$_2$/water ternary hybrid nanofluid under the combined effect of N_r and Γ_d is demonstrated in Fig. 6a,b. The outcomes noticeably display that an increase in the N_r and Γ_d leads to a substantial increase in the $\chi(\xi)$ within the boundary layer. This improvement is more pronounced in the ternary hybrid nanofluid compared to the hybrid nanofluid, showing the higher thermal transport potential of the ternary combination due to its improved thermal conductivity and synergistic nanoparticle interactions. Physically, the increase in the N_r improve radiative heat flux within the fluid domain, which served as an extra mode of energy transfer apart from conduction and convection. Likewise, the increase in the Γ_d parameter corresponds to a rise in volumetric energy discharge within the fluid system, thereby supplying to the internal thermal reservoir. Also, the effective surface area for energy absorption, thereby intensifying the impact of both N_r and Γ_d. Therefore, incorporating ternary CdTe-TiO_2-MoS_2/water ternary hybrid nanofluid in thermally intensive engineering applications can considerably improve productivity, reliability, and energy consumption.

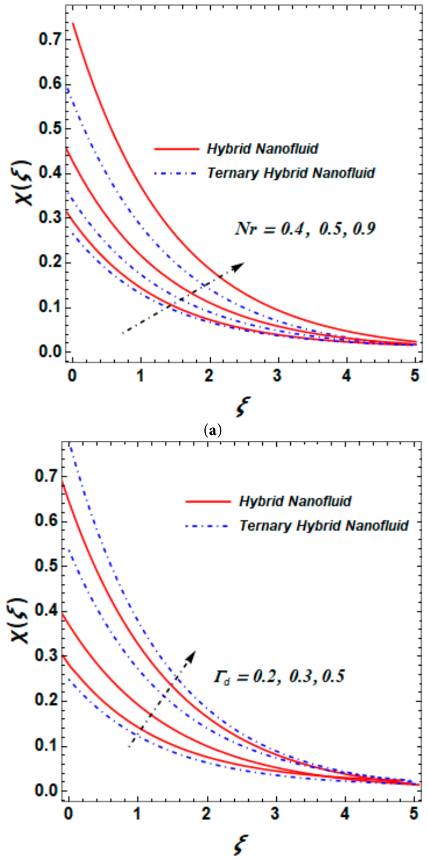

(a)

(b)

Figure 6: (**a**) Behavior of $\chi(\xi)$ under the effect of N_r. (**b**): Variation of $\chi(\xi)$ with Γ_d.

5 Conclusion

In this study, heat transport enhancement in magnetohydrodynamic flow of nanofluids containing TiO_2 (titanium dioxide), CdTe (cadmium telluride), and MoS_2 (molybdenum disulfide) nanoparticles over a vertical stretching/shrinking surface with thermal radiation has been analyzed. The study revealed that the interaction between electromagnetic forces, dissipation of viscous energy, and radiation intensity strongly governs both flow and heat transfer boundary layers. These results emphasize the potential of THNFs for advanced regulation of thermal energy, energy conversion, and heat removal systems, providing a theoretical basis for optimizing MHD thermal energy transfer in mechanical systems. Based on the numerical findings, the significant final remarks are outlined as follows:

- The M parameter exerts a retarding effect on the fluid motion, leading to a noticeable reduction in the fluid flow due to the Lorentz force opposing the flow.
- Greater values of the Gr_b increase the fluid flow, confirming the dominance of buoyancy-driven forces that encourage stronger convective currents.
- The Σ_d parameter positively impacts the velocity distribution, increasing the speed near the boundary region.
- The M, Ec_d, N_r, Γ_d parameters all contribute to advancement in the fluid temperature, increasing thermal energy within the boundary layer.
- Improved Ec_d values reveal the conversion of kinetic energy into internal energy through viscous dissipation, resulting in greater thermal distribution.
- The rise in N_r improves thermal transport and increases the thermal boundary layer thickness.
- The ternary hybrid nanofluid consistently displays greater improvement in both fluid flow compared with the hybrid nanofluid, owing to enriched thermal conductivity and synergistic particle interaction.
- The combined effect of electromagnetic forces, buoyancy influence, and internal heat sources plays an important function in determining the speed and thermal distribution performance.
- Practical usage of this research includes thermal management in magnetohydrodynamic (MHD) generators, microelectronic cooling systems, heat exchangers solar collectors, and nuclear reactor.

Limitations and Future Research

Despite the valuable insights provided by this study, some limitations should be acknowledged. First, the analysis is based on a steady, laminar, and two-dimensional flow assumption, which may not fully capture transient effects, turbulence, or three-dimensional behaviors encountered in practical engineering applications. Second, the thermophysical properties of the ternary hybrid nanofluid are assumed to be constant, whereas in reality they may vary with temperature, nanoparticle concentration, agglomeration, and shear rate. In addition, nanoparticle shape, size distribution, and possible slip mechanisms such as Brownian motion and thermophoresis are neglected. The porous medium is modeled as homogeneous and isotropic using the Darcy–Brinkman formulation, which may oversimplify complex porous structures found in real systems. Moreover, the study is purely numerical and lacks experimental or industrial validation to corroborate the predicted trends.

Future research may extend the present work by considering unsteady, three-dimensional, and turbulent flow configurations, as well as temperature-dependent and concentration-dependent fluid properties. Incorporating nanoparticle interaction effects, variable magnetic fields, non-uniform heat sources, and more realistic porous media models would further enhance the physical relevance of the model. Experimental studies or high-fidelity numerical simulations could be conducted to validate the theoretical predictions. Additionally, coupling the present framework with optimization techniques or machine-learning approaches could provide deeper insight into optimal parameter ranges for advanced thermal management and energy systems.

Acknowledgement: Not applicable.

Funding Statement: The authors received no specific funding for this study.

Author Contributions: Adebowale Martins Obalalu: Conceptualization, methodology, software, formal analysis, validation; writing—original draft, data curation, visualization. Umair Khan: Conceptualization, writing—original

draft, writing–review & editing, supervision, resources. Abdulazeez Adebayo Usman: Validation, investigation, writing—review & editing, formal analysis; project administration; funding acquisition. All authors reviewed and approved the final version of the manuscript.

Availability of Data and Materials: The datasets used and/or analyzed during the current study are available from the corresponding author upon reasonable request.

Ethics Approval: Not applicable.

Conflicts of Interest: The authors declare no conflicts of interest.

References

1. Behera US, Sangwai JS, Byun HS. A comprehensive review on the recent advances in applications of nanofluids for effective utilization of renewable energy. Renew Sustain Energy Rev. 2025;207:114901. [CrossRef].
2. Kumar Ahirwar B, Kumar A. A comprehensive review on heat transfer enhancement in tubular heat exchangers using twisted tapes, wire coil inserts, and their combined effect with nanofluids. Renew Sustain Energy Rev. 2025;224:116035. [CrossRef].
3. Razzaq I, Wang X, Rasool G, Tao S, Shflot AS, Malik MY, et al. Nanofluids for advanced applications: A comprehensive review on preparation methods, properties, and environmental impact. ACS Omega. 2025;10(6):5251–82. [CrossRef].
4. Zou Q, Ma T, Liang J, Xu B, Ran Q. Mesomechanical weakening mechanism of coal modified by nanofluids with disparately sized SiO_2 nanoparticles. Int J Rock Mech Min Sci. 2025;188:106056. [CrossRef].
5. Venkateswarlu B, Chavan S, Joo SW, Kim SC, Nisar KS. A numerical investigation of heat transfer performance in a prismatic battery cooling system using hybrid nanofluids. Case Stud Therm Eng. 2025;66:105719. [CrossRef].
6. Mohamed Galal A, Martins Obalalu A, Akindele AO, Khan U, Usman AA, Olayemi OA, et al. Thermal performance of entropy-optimized tri-hybrid nanofluid flow within the context of two distinct non-Newtonian models: Application of solar-powered residential buildings. Comput Model Eng Sci. 2025;142(3):3089–113. [CrossRef].
7. Kotnurkar AS, Kallolikar N, Souayeh B. Metachronal ciliary wave motion analysis on peristaltic flow of hyperbolic tangent nanofluid through an inclined magnetic field in a symmetric channel. Int J Model Simul. 2025;45(1):280–92. [CrossRef].
8. Ahmad Lone S, Raizah Z, Alrabaiah H, Shahab S, Saeed A, Khan A. Exploring convective conditions in three-dimensional rotating ternary hybrid nanofluid flow over an extending sheet: A numerical analysis. J Therm Anal Calorim. 2025;150(4):2651–66. [CrossRef].
9. Khan I, Ahmed Khan MW. Artificial neural networking for computational assessment of ternary hybrid nanofluid flow caused by a stretching sheet: Implications of machine-learning approach. Eng Appl Comput Fluid Mech. 2024;18(1):2411786. [CrossRef].
10. Ali Pasha A, Al Mesfer MK, Kareem MW, Kodi R, Danish M, Patil S, et al. Effects of rotational forces, and thermal diffusion on unsteady magnetohydrodynamic (MHD) flow of a viscoelastic fluid through porous media with isothermal inclined plates. Case Stud Therm Eng. 2025;69:105977. [CrossRef].
11. Hussein UN, Khashi'ie NS, Arifin NM, Pop I. Magnetohydrodynamics (MHD) flow of ternary nanofluid and heat transfer past a permeable cylinder with velocity slip. Chin J Phys. 2025;93:328–39. [CrossRef].
12. Hussein SA, Ahmed SE, Arafa AAM. Ciliary peristalsis flow of hydromagnetic Sutterby nanofluid through symmetric channel: Viscous dissipation in case of variable electrical conductivity. Eng Sci Technol Int J. 2025;62:101956. [CrossRef].
13. Kumar B, Jangili S. Time-periodic electroosmotic flow of non-Newtonian fluid through a polyelectrolyte-grafted circular microchannel. Phys Fluids. 2025;37(3):032043. [CrossRef].
14. Ogunsanwo GO, Alaba OB, Obalalu AM, Isarinade AF, Khan U, Ghodhbani R, et al. Dynamics of second-law analysis and thermal performance in solar-powered tractors using a parabolic trough solar collector filled with tri-hybrid nanofluid. J Therm Anal Calorim. 2025;150(13):10513–28. [CrossRef].
15. Hussain SM, Obalalu AM, Khan U, Usman AA. Analysis of radiative non-Newtonian ternary hybrid nanofluid flow in a squeezed arterial channel with electroosmosis effects. Proc Inst Mech Eng Part N J Nanomater Nanoeng Nanosyst. 2025:23977914251345058. [CrossRef].

16. Adogbeji VO, Atofarati EO, Sharifpur M, Meyer JP. Magnetohydrodynamics of nanofluid internal forced convection: A review and outlook for practical applications. Results Phys. 2025;68:108082. [CrossRef].
17. Krishna MV. Hall and ion slip effects on radiative MHD rotating flow of Jeffreys fluid past an infinite vertical flat porous surface with ramped wall velocity and temperature. Int Commun Heat Mass Transf. 2021;126:105399. [CrossRef].
18. Ullah H, Abas SA, Fiza M, Jan AU, Akgul A, El-Rahman MA, et al. Thermal radiation effects of ternary hybrid nanofluid flow in the activation energy: Numerical computational approach. Results Eng. 2025;25:104062. [CrossRef].
19. Karthik K, J K M, Kiran S, K V N, Prasannakumara BC, Fehmi G. Impacts of thermophoretic deposition and thermal radiation on heat and mass transfer analysis of ternary nanofluid flow across a wedge. Int J Model Simul. 2025;45(5):1688–700. [CrossRef].
20. Eswaramoorthi S, Nasir S, Loganathan K, Gupta MS, Berrouk A. Numerical simulation of rotating flow of CNT nanofluids with thermal radiation, ohmic heating, and autocatalytic chemical reactions. Alex Eng J. 2025;113:535–50. [CrossRef].
21. Hussain SM, Khan U, Obalalu AM. Impact of axial electric and inclined magnetic fields on tri-hybrid nanofluid through an electroosmotic flexible pump for biomedical microfluidic devices. Chem Phys Impact. 2025;11:100902. [CrossRef].
22. Sarkar S, Das S. Dynamics of oxytactic microbes-infused cross nanofluid around a stretchy cylinder subject to Lorentz force, Arrhenius activation energy, and nonlinear thermal radiation. Eur Phys J Plus. 2024;139(2):120. [CrossRef].
23. Kanwal S, Ali Shah SA, Bariq A, Ali B, Ragab AE, Az-Zo'bi EA. Insight into the dynamics of heat and mass transfer in nanofluid flow with linear/nonlinear mixed convection, thermal radiation, and activation energy effects over the rotating disk. Sci Rep. 2023;13:23031. [CrossRef].
24. Elattar S, Khan U, Zaib A, Ishak A, Alwadai N, Albalawi H. External velocity and dissipative flow of clay nanoparticles on the lubricity of drilling fluids across a vertical surface in a Darcy-Brinkman porous medium with thermal radiation. J Mol Liq. 2024;409:125428. [CrossRef].
25. Ali A, Mahrous YM, Elmannai H, Abduvalieva D, Karmakar P, Das S. Neuro-computational dynamics of an electromagnetically reactive copper-titania-water mixture within a quadratically accelerated Riga channel with graduated thermo-solutal conditions. Int Commun Heat Mass Transf. 2025;169:109666. [CrossRef].
26. Fatima N, Ali A, Das S, Almubaddel FS, Bentalib A, Orlova T. Electromagnetic influences on fractional hemodynamics of trihybrid nanolayered nanoparticles in a diverging ciliated microtube: A machine learning-assisted analysis for biomedical applications. J Comput Appl Math. 2026;474:116929. [CrossRef].
27. Uddin MJ, Rahman MM. Buoyancy-driven magnetohydrodynamic nanofluid flow and heat transfer in a porous cavity with an exothermic reaction governed by Arrhenius kinetics. Hybrid Adv. 2026;12:100594. [CrossRef].
28. Uddin MJ, Al Kalbani KS, Rahman MM, Alam MS, Al-Salti N, Eltayeb I. Fundamentals of nanofluids: Evolution, applications and new theory. Int J Biomath Syst Biol. 2016;2(1):1–32.
29. Rahman M, Uddin J. Magnetohydrodynamic boundary layer flow of nanofluid with variable chemical reaction in a radiative vertical plate. Heat Transf. 2021;50(8):7879–97. [CrossRef].
30. Kazaz O, Abu-Nada E. Latent heat-assisted thermal management of a metal hydride hydrogen storage reactor using novel shape-stabilized composite phase change material slurry. Energy Convers Manag. 2026;350:121000. [CrossRef].
31. Kazaz O, Abu-Nada E. Photothermal-responsive form-stable phase change materials for enhanced solar absorption and evaporation in advanced desalination systems. Appl Therm Eng. 2025;279:127842. [CrossRef].
32. Ishak A, Nazar R, Pop I. Mixed convection on the stagnation point flow toward a vertical, continuously stretching sheet. J Heat Transf. 2007;129(8):1087–90. [CrossRef].
33. Das S, Chakraborty S, Jana RN, Makinde OD. Entropy analysis of unsteady magneto-nanofluid flow past accelerating stretching sheet with convective boundary condition. Appl Math Mech Engl Ed. 2015;36(12):1593–610. [CrossRef].